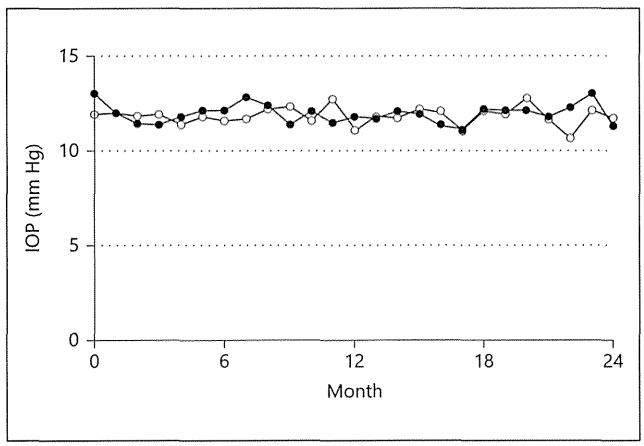

Fig. 3. The mean monthly IOP values of the eyes injected with IVR (closed circles) and the fellow eyes (open circles) in patients with AMD and glaucoma. The highest mean IOP of the injected eyes during the follow-up period is 13.0 ± 4.0 mm Hg at month 23, which does not differ significantly from the mean baseline IOP. There is no significant difference in the mean IOP between the treated eyes and the control fellow eyes.

Discussion

In the current study, no sustained IOP elevation occurred in any eyes treated with paracentesis just before intravitreal injections of ranibizumab. Good et al. [12] found that sustained IOP elevation (defined similarly to the above definition) developed in 3 of 96 eyes (3.1%) after IVR injections without paracentesis. Wehrli et al. [14] reported that a sustained IOP elevation or 1 IOP elevation exceeding 26 mm Hg occurred in 1 eye of 104 (1%) after IVR injections without paracentesis during 2 years of follow-up. Menke et al. [15] reported that the mean IOP was elevated significantly by 0.8 ± 3.1 mm Hg after IVR injections without paracentesis ($p < 0.0001$). The prevalence of sustained IOP elevations was lower in the current than in previous studies [12–14] and the highest mean IOP during the follow-up period was not significantly elevated from baseline. Furthermore, there was no significant difference in the mean IOP between the treated eyes and the control fellow eyes in this study. Although unclear, the reason for the absence of sustained IOP elevation in the current study could be that anterior chamber paracentesis was performed just before injecting ranibizumab. Paracentesis might prevent damage to outflow pathways due to IOP spikes associated with the injection procedure. Therefore it would be better to perform paracentesis to prevent IOP spikes and sustained IOP elevation.

Transient IOP elevations were found in 4 eyes in the current study but the frequency of IVR injections was not associated with transient IOP elevation.

No patients with AMD and glaucoma (n = 9) in the current study developed sustained IOP elevation. The percentages of sustained IOP elevations in patients with glaucoma have varied widely in previous studies [12–15]. Wehrli et al. [14] also found no patients with AMD and glaucoma who developed a sustained IOP elevation or had an IOP elevation that exceeded 26 mm Hg. In contrast, Good et al. [12] reported that 33% of patients with AMD and glaucoma developed sustained IOP elevations after IVR and/or intravitreal bevacizumab (IVB) injections. A possible reason for this variability might be due to the small sample size and variations in glaucoma types and severities.

Bevacizumab has also been used widely as an off-label treatment for neovascular AMD, retinal vein occlusion and diabetic retinopathy. Several previous studies have reported sustained IOP elevations after IVB injections [12, 13]. In the study of Good et al. [12], 10 (9.9%) of 101 patients developed sustained IOP elevations after IVB injections; in the study of Mathalone et al. [13], 22 (11%) of 201 patients developed sustained IOP elevations after IVB injections. These data suggested that the risk of developing sustained IOP elevations might be higher after IVB injections than after IVR injections.

What accounts for the difference between the rate of sustained IOP elevation prevalence after IVR injections and that after IVB injections is unclear. One possible reason could be the difference in molecular weight between ranibizumab (48 kDa) and bevacizumab (149 kDa). Being a full-length antibody, bevacizumab diffuses slowly into the anterior chamber and clears slowly from the vitreous cavity [18]. Therefore, Jalil et al. [19] hypothesized that bevacizumab accumulation in the trabeculum leads to aqueous outflow resistance and acute rise in IOP. Another possible mechanism for the development of sustained IOP elevations may be associated with the repackaging of bevacizumab in plastic syringes and extended storage times of the drug [12–14], which may lead to aggregation of proteins and/or nonproteinaceous materials such as silicone oil from the syringes. These aggregates can mechanically obstruct aqueous outflow [20, 21]. This might also explain the higher prevalence of IOP elevations after IVB injections than after IVR injections reported by previous studies. In support of that hypothesis, Wehrli et al. [14] found that IVR and/or IVB injections were not associated with an increased risk for IOP elevations when silicone-free syringes were used and the drugs were stored for less than 2 weeks before use. Although

silicone-coated syringes were used for ranibizumab injection in the current study, no eye developed sustained IOP elevation. One possible reason is that we repackaged ranibizumab on site just prior to injection. However, Mathalone et al. [13] found that 11% of patients developed sustained IOP elevations after injections of IVB stored for just a short time (up to 3 days). In addition, Menke et al. [15] reported a clear tendency to increased IOP in eyes with longer treatment duration using nonrepackaged drugs. Therefore, reasons other than silicone oil for sustained IOP elevation after anti-VEGF injection should be considered.

The limitations of the current study were its retrospective nature and the method of measuring the IOP, which differed from the Goldmann applanation tonometry method used in previous reports [12–15]. Several studies have reported moderate agreement between normal IOP levels measured by noncontact tonometry and Goldmann applanation tonometry [22, 23]. In the current study, no patients had extremely high or low IOP values, so we considered that our results were comparable with previously reported results [12–15].

In conclusion, repeated injections of ranibizumab with anterior chamber paracentesis seem not to be associated with an increased risk of IOP elevation. Anterior chamber paracentesis before IVR injections might prevent sustained IOP elevation.

Disclosure Statement

This paper was supported in part by a grant from the Ministry of Education, Culture, Sports, Science and Technology of Japan (No. 24592668). Shiga University of Medical Science and Dr. Ohji have received financial support from Novartis Pharmaceuticals Japan that is not directly related with this article. All the other authors declare no conflict of interest.

References

1 Rosenfeld PJ, Brown DM, Heier JS, Boyer DS, Kaiser PK, Chung CY, Kim RY: Ranibizumab for neovascular age-related macular degeneration. N Engl J Med 2006;355:1419–1431.
2 Brown DM, Kaiser PK, Michels M, Soubrane G, Heier JS, Kim RY, Sy JP, Schneider S: Ranibizumab versus verteporfin for neovascular age-related macular degeneration. N Engl J Med 2006;355:1432–1444.
3 Gragoudas ES, Adamis AP, Cunningham ET Jr, Feinsod M, Guyer DR; VEGF Inhibition Study in Ocular Neovascularization Clinical Trial Group: Pegaptanib for neovascular age-related macular degeneration. N Engl J Med 2004;351:2805–2816.
4 Heier JS, Brown DM, Chong V, Korobelnik JF, Kaiser PK, Nguyen QD, Kirchhof B, Ho A, Ogura Y, Yancopoulos GD, Stahl N, Vitti R, Berliner AJ, Soo Y, Anderesi M, Groetzbach G, Sommerauer B, Sandbrink R, Simader C, Schmidt-Erfurth U; VIEW 1 and VIEW 2 Study Groups: Intravitreal aflibercept (VEGF trap-eye) in wet age-related macular degeneration. Ophthalmology 2012;119:2537–2548.
5 Zondor SD, Medina PJ: Bevacizumab: an angiogenesis inhibitor with efficacy in colorectal and other malignancies. Ann Pharmacother 2004;38:1258–1264.
6 Kahook MY, Kimura AE, Wong LJ, Ammar DA, Maycotte MA, Mandava N: Sustained elevation in intraocular pressure associated with intravitreal bevacizumab injections. Ophthalmic Surg Lasers Imaging 2009;40:293–295.
7 Bakri SJ, McCannel CA, Edwards AO, Moshfeghi DM: Persistent ocular hypertension following intravitreal ranibizumab. Graefes Arch Clin Exp Ophthalmol 2008;246:955–958.
8 Adelman RA, Zheng Q, Mayer HR: Persistent ocular hypertension following intravitreal bevacizumab and ranibizumab injections. J Ocul Pharmacol Ther 2010;26:105–110.
9 Loukianou E, Brouzas D, Apostolopoulos M: Sustained ocular hypertension following intravitreal injections of 0.5 mg/0.05 ml ranibizumab. Int Ophthalmol 2011;31:211–213.
10 Tseng JJ, Vance SK, Della Torre KE, Mendonca LS, Cooney MJ, Klancnik JM, Sorenson JA, Freund KB: Sustained increased intraocular pressure related to intravitreal antivascular endothelial growth factor therapy for neovascular age-related macular degeneration. J Glaucoma 2012;21:241–247.
11 Hoang QV, Mendonca LS, Della Torre KE, Jung JJ, Tsuang AJ, Freund KB: Effect on intraocular pressure in patients receiving unilateral intravitreal anti-vascular endothelial growth factor injections. Ophthalmology 2012;119:321–326.
12 Good TJ, Kimura AE, Mandava N, Kahook MY: Sustained elevation of intraocular pressure after intravitreal injections of anti-VEGF agents. Br J Ophthalmol 2011;95:1111–1114.
13 Mathalone N, Arodi-Golan A, Sar S, Wolfson Y, Shalem M, Lavi I, Gever O: Sustained elevation of intraocular pressure after intravitreal injections of bevacizumab in eyes with neovascular age-related macular degeneration. Graefes Arch Clin Exp Ophthalmol 2012;250:1435–1440.
14 Wehrli SJ, Tawse K, Levin MH, Zaidi A, Pistilli M, Brucker AJ: A lack of delayed intraocular pressure elevation in patients treated with intravitreal injection of bevacizumab and ranibizumab. Retina 2012;32:1295–1301.
15 Menke MN, Salam A, Framme C, Wolf S: Long-term intraocular pressure change in patients with neovascular age-related macular degeneration treated with ranibizumab. Ophthalmologica 2013;229:168–172.
16 Tano Y, Ohji M, Ishibashi T, Shiraga F, Tokoro T, Yuzawa M, Yoshimura N: Re-treatment guideline of ranibizumab (genetical recombination) in the maintenance phase. Nihon Ganka Gakkai Zasshi 2009;113:1098–1103.
17 Drance SM: The significance of the diurnal tension variations in normal and glaucomatous eyes. Arch Ophthalmol 1960;64:494–501.
18 Krohne TU, Eter N, Holz FG, Meyer CH: Intraocular pharmacokinetics of bevacizumab after a single intravitreal injection in humans. Am J Ophthalmol 2008;146:508–512.
19 Jalil A, Fenerty C, Charles S: Intravitreal bevacizumab (Avastin) causing acute glaucoma: an unreported complication. Eye 2007;21:1541.
20 Liu L, Ammar DA, Ross LA, Mandava N, Kahook MY, Carpenter JF: Silicone oil microdroplets and protein aggregates in repackaged bevacizumab and ranibizumab: effects of long-term storage and product mishandling. Invest Ophthalmol Vis Sci 2011;52:1023–1034.
21 Kahook MY, Liu L, Ruzycki P, Mandava N, Carpenter JF, Petrash JM, Ammar DA: High-molecular-weight aggregates in repackaged bevacizumab. Retina 2010;30:887–892.
22 Packer VA, Herrtage J, Sarkies NJ: Clinical comparison of the Keeler Pulsair 3000 with Goldman applanation tonometry. Br J Ophthalmol 2001;85:1303–1304.
23 Tonnu P-A, Ho T, Sharma K, White E, Bunce C, Garway-Heath D: A comparison of four methods of tonometry: method agreement and interobserver variability. Br J Ophthalmol 2005;89:847–850.

Acta Ophthalmologica

Analysis of retinal vessels in eyes with retinitis pigmentosa by retinal oximeter

Tomoko Ueda-Consolvo, Chiharu Fuchizawa, Mitsuya Otsuka, Takuya Nakagawa and Atsushi Hayashi

Department of Ophthalmology, Graduate School of Medicine and Pharmaceutical Sciences, University of Toyama, Toyama, Japan

ABSTRACT.

Purpose: **To study changes in the oxygen saturation and calibre of retinal vessels in the eyes of patients with retinitis pigmentosa (RP).**

Method: **In this cross-sectional study, 63 eyes of 63 patients with RP and 14 eyes of 14 healthy subjects were enrolled and examined at Toyama University Hospital. Retinal oximetry measurements were performed using a spectrophotometric oximetry unit (Oxymap T1, Reykjavik, Iceland), which is coupled to a fundus camera base (TRC-50DX; Topcon Corporation, Tokyo, Japan). Retinal arterioles of 28 eyes and retinal venules of 35 eyes with adequate image quality were selected for analyses. We calculated the residual areas of visual field (I-4e and V-4e isopters) in each eye and determined the correlations between the data of retinal vessels and the areas of visual field in the RP eyes.**

Results: **The mean oxygen saturation of the venules in the RP eyes (60.2 ± 6.5%) was significantly higher than that in healthy eyes (54.6 ± 6.3%, $p = 0.0089$). The oxygen saturation of the venules in the RP eyes correlated significantly with the residual areas of the visual field of V-4e ($r = -0.50$; $p = 0.0030$). The mean calibres of the retinal arterioles (91.1 ± 9.1 μm) and retinal venules (116 ± 13 μm) of the RP eyes were significantly narrower than those of the healthy eyes (115 ± 11 μm and 152 ± 15 μm, respectively, $p < 0.01$). The retinal arteriolar and venular calibres in the RP eyes correlated with the residual areas of the visual field of V-4e ($r = 0.43$; $p = 0.033$ and $r = 0.45$; $p = 0.011$, respectively).**

Conclusions: **The severity of RP was correlated with increased oxygen saturations in the retinal venules and decreased retinal vessel calibres.**

Key words: oxygen saturation – retinal oximeter – retinal vessels – Retinitis pigmentosa – vessel calibre – visual field

Acta Ophthalmol.

doi: 10.1111/aos.12597

Introduction

Retinitis pigmentosa (RP) is not a rare disease: it affects about 1 in 4000 people (Hartong et al. 2006). Patients typically notice progressive deterioration in night vision in their adolescence, followed by loss of the mid-peripheral visual field in young adulthood. The progressive degeneration of rod and cone photoreceptors leads to tunnel vision and finally the loss of central vision. RP is known to be inherited in an autosomal dominant (30–40%), autosomal recessive (50–60%) or X-linked (5–15%) pattern. Some cases are sporadic and lack a family history of the disease (Hartong et al. 2006).

Characteristic findings in the fundus with RP are bone–spicule deposits in the mid-periphery or far periphery of the retina, waxy pallor optic disc and attenuation of retinal vessels. The oxygen metabolic changes in the retina of a patient with RP are still unclear. Ma et al. (2012) showed that the retinal vessel attenuation was associated with the severity of RP assessed as visual field area. Their results indicated that retinal vessel attenuation reflected decreased metabolic demands of the degenerated retina. Yu & Cringle (2005) reported that the intraretinal oxygen distribution changed in the outer retina during the degeneration of photoreceptors in rat models. It is, however, difficult to study *in vivo* changes in the oxygen saturations of a patient's retina non-invasively.

A spectrophotometric retinal oximeter, the Oxymap T1 (Oxymap, Reykjavik, Iceland), was developed and used for non-invasive examinations of the oxygen saturations and calibres of retinal vessels affected by diseases such as glaucoma, retinal vein occlusion and diabetic retinopathy (Hardarson & Stefánsson 2010, 2012; Olafsdottir et al. 2011; Vandewalle et al. 2014). Three groups reported changes in the oxygen saturation of retinal vessels in patients with RP (Eysteinsson et al. 2014; Todorova et al. 2014; Turksever et al. 2014). They used the Oxymap T1 or an oximetry tool of retinal vessel analyser and showed that the oxygen saturations of retinal venules were higher in RP eyes than in healthy eyes. In this study, we non-invasively measured the oxygen saturations and calibres of retinal arterioles and venules using the Oxymap T1, and we investi-

gated the correlations between these data and residual areas of the visual field in patients with RP.

Methods

Inclusion/exclusion criteria for RP

We enrolled and examined 63 eyes of 63 consecutive patients with RP, who visited Toyama University Hospital between October 2012 and September 2013. Inclusion criteria were (1) patients with the diagnosis of retinitis pigmentosa by fundus appearances and reduced amplitudes of electroretinograms, (2) patients without previous intra-ocular surgeries due to cataract, glaucoma and vitreoretinal diseases, and (3) patients without advanced cataract, corneal opacity or vitreous haemorrhage which disturbed to take fundus photographs. We excluded blurred or partially dark vessels with poor image quality due to cataract or small pupil from further analyses. We also excluded the image with too bright background due to degeneration.

Inclusion/exclusion criteria for control

Exclusion criteria for healthy subjects were having any history of retinal or optic nerve diseases, glaucoma, eye trauma, diabetes mellitus or any cardiovascular or respiratory diseases. Fourteen healthy Japanese persons were recruited for the study. Seven of the 14 healthy subjects came to our hospital because of symptoms of vitreous floaters. The other seven healthy subjects were volunteers in our hospital. The healthy subjects matched in age and gender with the patients with RP (Table 1).

Ophthalmic examinations

All patients and healthy controls underwent comprehensive ophthalmologic examinations, including measurement of the best-corrected decimal visual acuity and intra-ocular pressure, and slit- lamp biomicroscopy. All patients with RP and six healthy subjects underwent a visual field test using a Goldmann perimeter (Haag Streit, Bern, Switzerland).

To measure the oxygen saturation and calibre of the participants' retinal vessels, we used a spectrophotometric oximetry unit (Oxymap T1; Oxymap), which is coupled to a fundus camera base (TRC-50DX; Topcon Corporation, Tokyo, Japan) with a specialized software (oxymap analyser software 2.4.0; Oxymap).

Table 1. Clinical characteristics of retinitis pigmentosa (RP) patients and healthy subjects.

	RP		Healthy subjects		
Enrolled (patients/eyes)	63/63		14/14		
Selected arterioles (patients/eyes)					
Male	12/12		6/6		p = 1.0
Female	16/16		8/8		
Selected venules (patients/eyes)					
Male	15/15		6/6		p = 1.0
Female	20/20		8/8		
	Mean ± SD	95%CI	Mean ± SD	95%CI	
Age	52 ± 15	46–58	43 ± 17	33–53	p = 0.07
Decimal BCVA	0.33		1.5		
Duration of RP (years)	14.9 ± 11.3	11.6–18.1			
Number of retinal arteries per eye	2.2 ± 0.9	1.9–2.5	6.5 ± 0.7	6.1–6.9	
Number of retinal venules per eye	3.1 ± 0.9	2.8–3.4	6.6 ± 1.2	5.9–7.3	
Visual field area (V-4e) cm^2	63 ± 60	42–84	204 ± 3.0	203–205	
Visual field area (I-4e) cm^2	10 ± 19	3–17	125 ± 15	118–132	
Oxygen saturation of arterioles (%)	102 ± 8.9	98.9–105.9	99.9 ± 8.9	94.7–105.0	p = 0.31
Oxygen saturation of venules (%)	60.2 ± 6.5	58.0–62.4	54.6 ± 6.3	50.9–58.2	p = 0.0089
Caliber of the retinal arterioles (μm)	91.1 ± 9.1	87.6–94.6	115 ± 11	109–121	<0.01
Caliber of the retinal venules (μm)	116 ± 13	111–121	152 ± 15	143–161	<0.01

BCVA = best-corrected visual acuity; SD = standard deviation; 95%CI = 95% confidence interval.

Research protocol

The research protocol was approved by the Institutional Review Board of the University of Toyama, and the procedures used conformed to the tenets of the Declaration of Helsinki. After the nature and possible consequences of the study were explained to the patients and healthy subjects, written informed consent was obtained from each subject.

Analyses

We calculated the areas of I-4e and V-4e isopters in each visual field using ImageJ software (National Institutes of Health, Bethesda, MD; available at http://imagej.nih.gov/ij/).

wWe analysed the vessel segments according to the protocol specified by Geirsdottir et al. (2012). Only images with adequate quality with the optic disc located in the centre were used for analysis. Briefly, the retinal vessel width was eight pixels or wider, the length was 50–200 pixels, and the vessel measurement started from more than 15 pixels next to the optic disc and ended after the length of 200 pixels. When vessel branching occurred, the branching was ignored if the vessel width was six pixels or less; if the vessel width was wider than six pixels, the analysis was started from the vessel branching. As the oxygen saturation, measured with a dual wavelength oximeter, was shown to decrease with increased vessel diameter (Beach et al. 1999), values of the oxygen saturation were adjusted with retinal vessel diameters by the software of Oxymap T1.

We used data of only one eye per each patient or healthy subject for statistical analyses.

Primary objective and secondary objective

Primary objective was to compare oxygen saturations and calibres of the retinal vessels between patients with RP and healthy controls. Secondary objective was to examine correlations between the residual areas of the visual field and the data of retinal oxygen saturation and vessel calibres in patients with RP.

Statistical analyses

The statistical analyses were carried out using JMP® statistical discovery

software (Version 9; SAS Institute, Cary, NC). Wilcoxon rank-sum test was used for comparisons of the two groups. Pearson's correlation procedure was used to examine statistical correlations. Statistical significance was defined as $p < 0.05$.

Results

The characteristics of the patients with RP and healthy volunteers are listed in Table 1. Fundus photographs were taken in all 63 eyes of the 63 patients by the Oxymap T1, and 28 eyes of 28 patients showed adequate image quality to analyse the oxygen saturations of retinal arterioles; 35 eyes of 35 patients showed adequate image quality to analyse the oxygen saturations of retinal venules. The decimal best-corrected visual acuity (BCVA) of the selected 35 patients with RP for analysis ranged from 0.01 to 1.5 (mean, 0.33). Mean periods after the diagnosis of RP were 14.9 ± 11.3 years (mean±standard deviation (SD), 95% confidence interval (CI), 11.6–18.1).

In the RP eyes, 2.2 ± 0.9 of arterioles (mean ± SD, 95% CI 1.9–2.5) per eye and 3.1 ± 0.9 of venules (mean ± SD, 95% CI, 2.8–3.4) per eye were analysed. In the healthy eyes, 6.5 ± 0.7 of arterioles (mean ± SD, 95% CI, 6.1–6.9) per eye and 6.6 ± 1.2 of venules (mean ± SD, 95% CI, 5.9–7.3) per eye were analysed (Table 1).

Figure 1A shows a typical colour fundus photograph of the left eye of a patient with RP. Figure 1B shows selected vessels for vessel analysis on a pseudo-colour-mapped fundus photograph of the same eye as shown in Fig. 1A, taken by the Oxymap T1. Because we analysed only vessels with 8 pixels or wider width to obtain reliable results, the numbers of analysed vessels were smaller in the RP eyes than in the healthy eyes. In the RP eyes, the nasal vessels were selected for analysis only in one eye. In the rest of the RP eyes, only temporal vessels were analysed.

In RP eyes, the mean residual area of the visual field of the I-4e isopter was 10 ± 19 cm^2 (mean ± SD, 95% CI, 3–17 cm^2, range, 0–78 cm^2) and the mean residual area of the visual field of the V-4e isopter was 63 ± 60 cm^2 (mean ± SD, 95% CI, 42–84 cm^2, range, 0.2–184 cm^2) (Table 1). We performed a visual field test for 6 healthy subjects and obtained consistent results which showed 204 ± 3.0 cm^2 of V-4e (mean ± SD) and 125 ± 15 cm^2 of I-4e (mean ± SD). There was no correlation between the oximetry data and residual areas of visual field in healthy controls.

Oxygen saturation

As shown in Fig. 2A, the mean oxygen saturation in venules was significantly higher in the RP eyes (60.2 ± 6.5%, mean ± SD) than in the healthy eyes (54.6 ± 6.3%, mean ± SD; $p = 0.0089$). The mean oxygen saturation in arterioles in the RP eyes (102 ± 8.9%) was not significantly different from that in the healthy eyes (99.9 ± 8.9%, mean ± SD, $p = 0.31$, Fig. 2B).

In the RP eyes, the oxygen saturations of the retinal venules correlated with the residual areas of visual field measured by V-4e isopter (Pearson's correlation coefficients, $r = -0.50$; $p = 0.0030$; $n = 35$) (Fig. 3). There was no correlation between the oxygen saturations of retinal venules and the visual field area of the I-4e isopter ($r = -0.23$ $p = 0.19$; $n = 35$). No correlation was detected between the oxygen saturations of the retinal arterioles and the residual areas of visual field of V-4e ($r = -0.19$; $p = 0.35$; $n = 28$) or I-4e ($r = -0.05$; $p = 0.82$; $n = 28$).

Retinal vessel calibre

As shown in Fig. 4A, the mean calibre of the retinal venules was significantly narrower in the RP eyes (116 ± 13 μm)

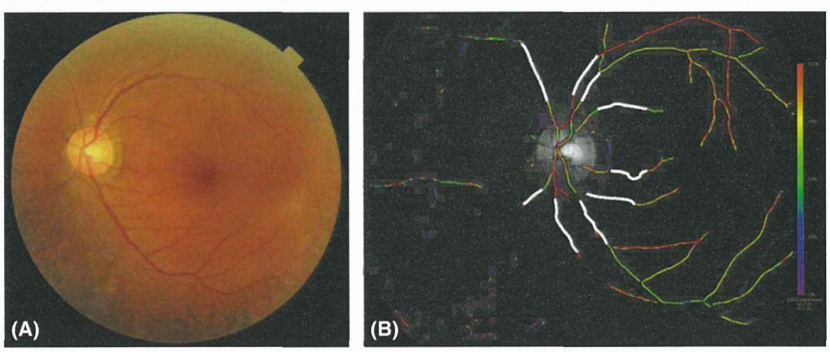

Fig. 1. (A) A colour fundus photograph of a patient with retinitis pigmentosa (RP). (B) A pseudo-colour map fundus photograph of the same RP eye as in (A). The Oxymap T1 showed selected vessel segments for analyses (white vessel segments).

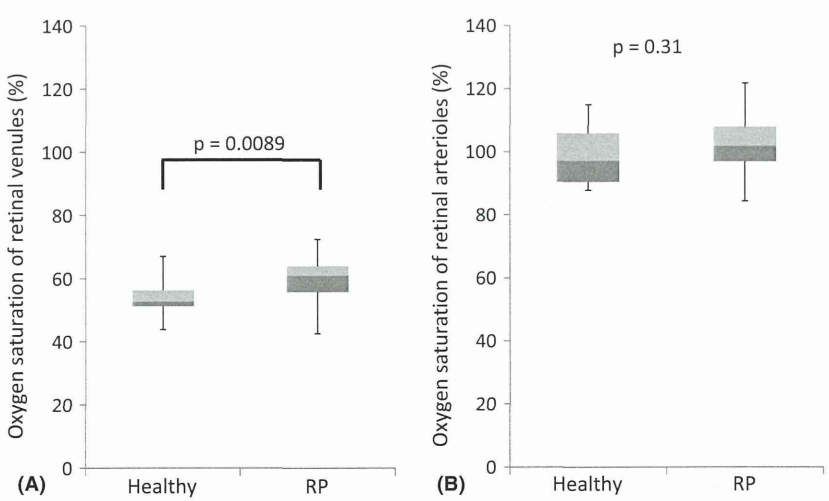

Fig. 2. (A) The mean oxygen saturations of retinal venules in the RP eyes and healthy eyes. The mean oxygen saturation was significantly higher in the RP eyes (60.2 ± 6.5%) than in the healthy eyes (54.6 ± 6.3%, $p = 0.0089$). (B) The mean oxygen saturation of retinal arterioles in the RP eyes and healthy eyes. There was no significant difference.

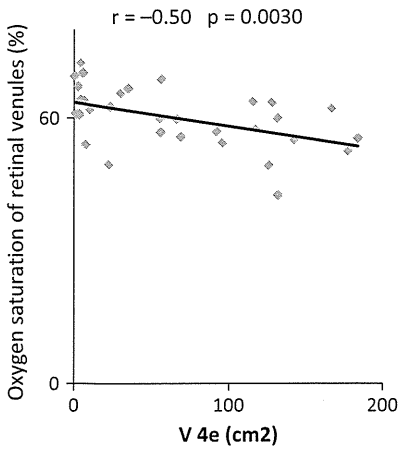

Fig. 3. Correlation between oxygen saturations of retinal venules and residual areas of the visual field of V-4e in the RP eyes (r = –0.50, p = 0.0030, n = 35).

than in the healthy eyes (152 ± 15 μm; p < 0.01). In addition, the mean calibre of the retinal arterioles was significantly narrower in the RP eyes (91.1 ± 9.1 μm) than in the healthy eyes (115 ± 11 μm; p < 0.01, Fig. 4B).

In the RP eyes, the retinal venular calibre correlated with the residual area of the visual field of V-4e isopter (r = 0.45; p = 0.011; n = 35) (Fig. 5). However, there was no correlation between the retinal venular calibre and the residual area of the visual field of the I-4e isopter (r = 0.15; p = 0.39; n = 35). The retinal arteriolar calibre correlated with the residual area of the visual field of V-4e in the RP eyes (r = 0.43; p = 0.033; n = 28) (Fig. 6). Similarly, there was no correlation between the retinal arteriolar calibre and the visual field area of I-4e (r = 0.087; p = 0.68; n = 28).

Discussion

Our present study agreed with recently published findings (Eysteinsson et al. 2014; Todorova et al. 2014; Turksever et al. 2014) that the oxygen saturation of the retinal venules was significantly higher in the RP eyes than in the healthy eyes. A novel finding in our study was that the oxygen saturation of the venules correlated with the residual area of the visual field of the RP eyes. These findings suggested that in the RP eyes, the retinal oxygen consumption was decreased due to the degeneration of the retina, especially the photoreceptors.

The Oxymap T1 retinal oximeter is useful for clinical studies because it non-invasively and quickly gives not only the oxygen saturations but also the calibres of retinal vessels (Hardarson & Stefánsson 2010, 2012; Olafsdottir et al. 2011; Geirsdottir et al. 2012; Vandewalle et al. 2014). Palsson et al. (2012) and Blondal et al. (2011) reported that measurements of retinal vessel oxygen saturation, and calibres with the Oxymap T1 were highly repeatable.

Yu & Cringle (2005) showed that the intraretinal oxygen distribution changed as the degeneration of photoreceptors progressed in a rat model. In the outer retina, oxygen levels were shown to increase as a result of the loss of photoreceptors, but the oxygen levels were not changed in the inner retina. Although there was a significant alteration in the oxygen flux from the choroid to the inner retina with the degeneration of photoreceptors (Yu & Cringle 2005; Padnick-Silver et al. 2006), normal oxygen levels in the inner retina were maintained. This may cause reduced oxygen input from

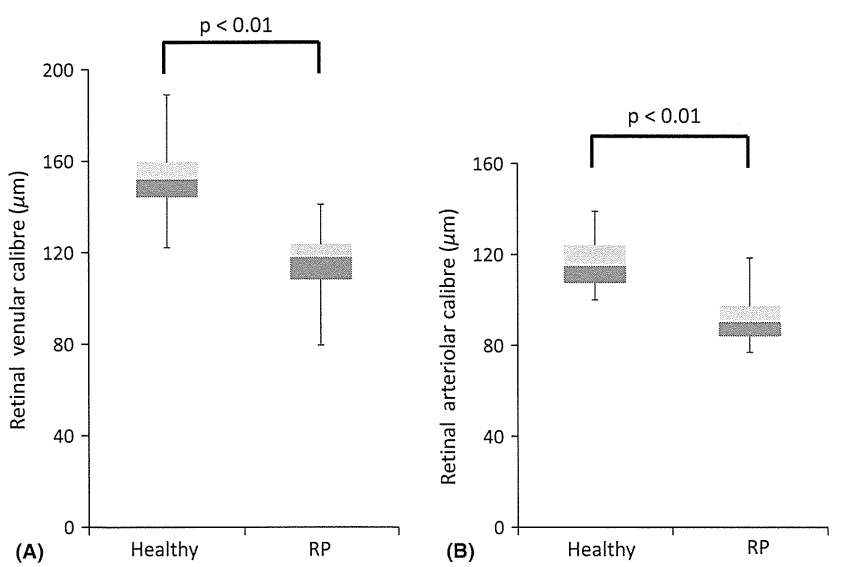

Fig. 4. The mean calibres of retinal venules (A) and arterioles (B) in the RP eyes and healthy eyes. The mean calibre of retinal venules was significantly narrower in the RP eyes (116 ± 13 μm) compared to the healthy eyes (152 ± 15 μm, p < 0.01). The mean calibre of retinal arterioles was significantly narrower in the RP eyes (91.1 ± 9.1 μm) than in the healthy eyes (115 ± 11 μm, p < 0.01).

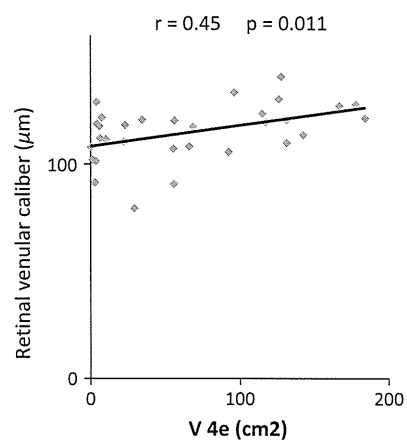

Fig. 5. Correlation between retinal venular calibres and residual areas of visual field of V-4e in the RP eyes (r = 0.45, p = 0.011, n = 35).

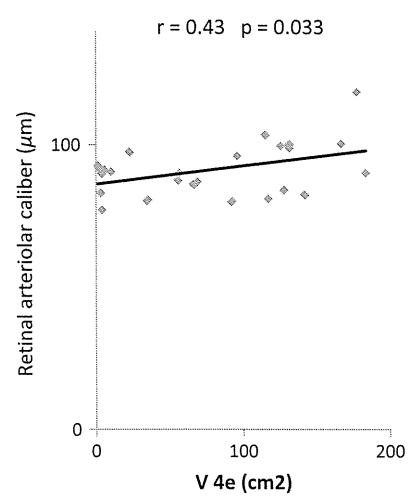

Fig. 6. Correlation between retinal arteriolar calibres and residual areas of visual field of V-4e in the RP eyes (r = 0.43, p = 0.033, n = 28).

the deeper capillary layer of the retinal circulation, which in turn, may cause narrowing of both the retinal arterioles and venules.

It is well known that both hypoxia and hyperoxia can cause neural cell stress and damage. Effective therapies for RP have not been identified. Some clinical and experimental studies demonstrated that hyperbaric oxygen therapy can be a safe approach to RP (Maslim et al. 1997; Vingolo et al. 1998–1999, 2008), although other studies showed that hypoxic therapy may be an avenue for slowing down the later stages of the retinal degeneration (Stone et al. 1999; Shen et al. 2005; Komeima et al. 2006). Our present results suggest that the oxygen saturations in the retinal venules of the RP eyes were higher than those of the healthy eyes and that additional oxygen may thus not be necessary for RP retinas.

Our study showed that retinal vessel calibres were reduced in RP eyes compared to healthy eyes. The average calibres of the retinal venules and arterioles in the RP eyes were narrower by 36 and 24 μm compared to those in the healthy eyes, respectively. Ma et al. (2012) reported that the mean central retinal artery and vein equivalent were decreased by -15.2 and -26.8 μm, respectively, per each 100 cm^2 decrease in visual field area and that the calibres of retinal arterioles and venules were weakly correlated with the residual area of the visual field of V-4e. Histopathologic studies showed that attenuation of the retinal blood vessels might result from not only degeneration of photoreceptors but also diminished ganglion cell metabolism (Milam et al. 1998).

The Oxymap T1 provides easy and reliable data regarding retinal vessel calibres and oxygen saturations for various retinal diseases, which will help elucidate retinal diseases from the viewpoint of retinal circulation, and this device will help determine the severity of retinal degeneration.

In conclusion, we found that the severity of RP was associated with increased oxygen saturation in retinal venules and decreased calibres of retinal arterioles and venules. Long-term studies are needed to examine the follow-up changes in oxygen saturation and vessel calibres in patients with RP and to classify the disease stages of the progressive retinal degeneration in the RP eyes.

References

Beach JM, Schwenzer KJ, Srinivas S et al. (1999): Oximetry of retinal vessels by dual-wavelength imaging: calibration and influence of pigmentation. J Appl Physiol **86**: 748–758.

Blondal R, Sturludottir MK, Hardarson SH, Halldorsson GH & Stefánsson E (2011): Reliability of vessel diameter measurements with a retinal oximeter. Graefes Arch Clin Exp Ophthalmol **249**: 1311–1317.

Eysteinsson T, Hardarson SH, Bragason D et al. (2014): Retinal vessel oxygen saturation and vessel diameter in retinitis pigmentosa. Acta Ophthalmol **92**: 449–453.

Geirsdottir A, Palsson O & Hardarson SH (2012): Retinal vessel oxygen saturation in healthy individuals. Invest Ophthalmol Vis Sci **53**: 5433–5442.

Hardarson SH & Stefánsson E (2010): Oxygen saturation in central retinal vein occlusion. Am J Ophthalmol **150**: 871–875.

Hardarson SH & Stefánsson E (2012): Retinal oxygen saturation is altered in diabetic retinopathy. Br J Ophthalmol **96**: 560–563.

Hartong DT, Berson E & Dryja TP (2006): Retinitis pigmentosa. Lancet **368**: 1795–1809.

Komeima K, Rogers BS, Lu L et al. (2006): Antioxidants reduce cone cell death in a model of retinitis pigmentosa. Proc Natl Acad Sci U S A **103**: 11300–11305.

Ma Y, Kawasaki R, Dobson LP et al. (2012): Quantitative analysis of retinal vessel attenuation in eyes with retinitis pigmentosa. Invest Ophthalmol Vis Sci **53**: 4306–4314.

Maslim J, Vaiter K, Egensperger R et al. (1997): Tissue oxygen during a critical development period controls the death and survival of photoreceptors. Invest Ophthalmol Vis Sci **38**: 1667–1677.

Milam AH, Li Z-Y & Fariss RN (1998): Histopathology of the human retina in retinitis pigmentosa. Prog Retin Eye Res **17**: 175–205.

Olafsdottir OB, Hardarson SH, Gottfredsdottir MS, Harris A & Stefánsson E (2011): Retinal oximetry in primary open-angle glaucoma. Invest Ophthalmol Vis Sci **52**: 6409–6413.

Padnick-Silver L, Kang Derwent JJ, Giuliano E et al. (2006): Retinal oxygen and oxygen metabolism in Abyssinian cats with a hereditary retinal degeneration. Invest Ophthalmol Vis Sci **47**: 3683–3689.

Palsson O, Geirsdottir A, Hardarson SH, Olafsdottir OB, Kristjansdottir JV & Stefánsson E (2012): Retinal oximetry images must be standardized: a methodological analysis. Invest Ophthalmol Vis Sci **53**: 1729–1733.

Shen J, Yang X, Dong A et al. (2005): Oxidative damage is a potential cause of cone cell death in retinitis pigmentosa. J Cell Physiol **203**: 457–464.

Stone J, Maslim J, Valter-Kocsi K et al. (1999): Mechanisms of photoreceptor death and survival in mammalian retina. Prog Retin Eye Res **18**: 689–735.

Todorova MG, Turksever C, Schorderet DF & Valmaggia C (2014): Retinal vessel oxygen saturation in patients suffering from inherited diseases of the retina. Klin Monbl Augenheilkd. **231**: 447–452.

Turksever C, Valmaggia C, Orgul S et al. (2014): Retinal vessel oxygen saturation and its correlation with structural changes in retinitis pigmentosa. Acta Ophthalmol **92**: 454–460.

Vandewalle E, Abegão Pinto L, Olafsdottir OB et al. (2014): Oximetry in glaucoma: correlation of metabolic change with structural and functional damage. Acta Ophthalmol **92**: 105–110.

Vingolo EM, Pelaia P, Forte R et al. (1998–1999): Does hyperbaric oxygen (HBO) delivery rescue retinal photoreceptors in retinitis pigmentosa. Doc Ophthalmol **97**: 33–39.

Vingolo EM, Rocco M, Grenga P et al. (2008): Slowing the degenerative process, long lasting effect of hyperbaric oxygen therapy in retinitis pigmentosa. Graefes Arch Clin Exp Ophthalmol **246**: 93–98.

Yu D-Y & Cringle SJ (2005): Retinal degeneration and local oxygen metabolism. Exp Eye Res **80**: 745–751.

Received on February 17th, 2014.
Accepted on October 12th, 2014.

Correspondence:
Atsushi Hayashi
Department of Ophthalmology Graduate School of Medicine and Pharmaceutical Science University of Toyama
2630 Sugitani
Toyama 930-0194, Japan
Tel: +81 76 434 7363
Fax: +81 76 434 5037
Email: ganka@med.u-toyama.ac.jp

Based on this model, we hypothesize that artificial administration of IGF-1 via RBC transfusions causes a misbalance in IGF-1 and VEGF levels, resulting in instant growth of neovascularizations in case of concomitant high levels of VEGF or postponement of neovascular growth when VEGF levels are low.

With this letter, we want to create more awareness for those infants delivered after TTTS who need high numbers of RBC transfusions. Although their peripheral retina may be largely vascularized, they can develop potentially blinding ROP in a rapid and progressive way and should therefore be monitored closely, so treatment can be performed in time, and blindness can be prevented.

References

Chen HL, Tseng HI, Lu CC, Yang SN, Fan HC Yang RC (2009): Effect of blood transfusions on the outcome of very low body weight preterm infants under two different transfusion criteria. Pediatr Neonatol **50**: 110–116.

Hellstrom A, Perruzzi C, Ju M *et al.* (2001): Low IGF-I suppresses VEGF-survival signaling in retinal endothelial cells: direct correlation with clinical retinopathy of prematurity. Proc Natl Acad Sci U S A **98**: 5804–5808.

Hubler A, Knote K, Kauf E, Barz D, Schlenvoigt D Schramm D (2006): Does insulin-like growth factor 1 contribute in red blood cell transfusions to the pathogenesis of retinopathy of prematurity during retinal neovascularization?Biol Neonate **89**: 92–98.

Puvanachandra N, Clifford L Gaston H (2009): Retinopathy of prematurity in twin-twin transfusion syndrome. J Pediatr Ophthalmol Strabismus **46**: 226–227.

Weintraub Z, Carmi N, Elouti H Rumelt S (2011): The association between stage 3 or higher retinopathy of prematurity and other disorders of prematurity. Can J Ophthalmol **46**: 419–424.

Correspondence:
Arlette J. van Sorge, MD and Prof. Nicoline E. Schalij-Delfos, MD, PhD
Leiden University Medical Centre
Department of Ophthalmology
P.O. Box 9600, 2300 RC Leiden, The Netherlands
Tel: + 31(0)71 5263938
Fax + 31(0)71 5248222
E-mails: a.j.van_sorge@lumc.nl and n.e.schalij-delfos@lumc.nl

Retinal images viewed through a small aperture corneal inlay

Makoto Inoue,[1,2] Hiroko Bissen-Miyajima,[2] Hiroyuki Arai[3] and Akito Hirakata[1]

[1]Kyorin Eye Center, Kyorin University School of Medicine, Tokyo, Japan; [2]Department of Ophthalmology, Tokyo Dental College Suidobashi Hospital, Tokyo, Japan; [3]Minatomirai Eye Clinic, Yokohama, Japan

doi: 10.1111/aos.12228

Editor,

Presbyopia is a visual disability of the ageing eye caused by a loss of accommodation of the crystalline lens (Charman 2008). To treat presbyopia, the Kamra corneal inlay (AcuFocus, Inc., Irvine, CA, USA) was designed with a small aperture, which increases the depth of focus (Yılmaz et al. 2011; Tomita et al. 2012). The inlay is 5 μm thick and incorporates carbon nanoparticles to create a 3.8-mm-diameter opaque sheet with a clear central aperture of 1.6 mm with zero refractive power (Yilmaz et al. 2008).

The inlay was reported not to affect the ophthalmoscopic view of the central and peripheral fundus, and high-quality central and peripheral fundus photographs and optical coherence tomographic (OCT) images could be obtained in eyes implanted with the inlay (Casas-Llera et al. 2011). However, it has not been determined how the inlay affects the retinal images when patients require vitreoretinal surgeries in eyes with dark-coloured rings in the centre of the cornea.

A 48-year-old woman visited Minatomirai Eye Clinic for symptomatic floaters in the left eye implanted with a Kamra cornea inlay. Routine retinal examination was performed, including a detailed retinal examination with a slit-lamp microscope and a Goldmann three-mirror contact lens (OG3MFA; Ocular Instruments, Washington, DC, USA) after the pupil was dilated by a topical mydriatic drug. Fundus photographs were taken with a retinal camera (Mark2 NW7SF; Topcon Corp, Tokyo, Japan) with a 50-degree angle and fundus images through a three-mirror contact lens with a slit-lamp microscope connected to a video camera mounted on a slit-lamp microscope.

The uncorrected decimal distant vision in the left eye of the patient implanted with the inlay was 1.2, and the uncorrected near vision was 0.8. The funduscopic images through the indirect ophthalmoscope and fundus photographed through the inlay were clear (Fig. 1). However, with a slit-lamp microscope, a blurred dark ring

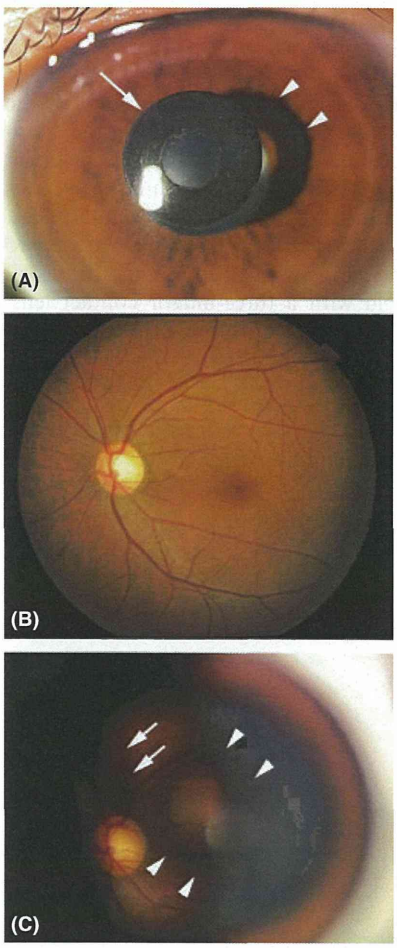

Fig. 1. Fundus images through a three-mirror contact lens with a slit-lamp microscope and a fundus camera in an eye implanted with the inlay. (A) A corneal inlay (arrow) is implanted in the centre of the cornea of the left eye. A shadow on the iris by the inlay is seen (arrowheads). (B) Fundus image is clear through the inlay. (C) A defocused dark ring (arrowheads) is seen through the three-mirror contact lens. A shadow cast (arrows) on the retina by the inlay is also seen.

was observed through the centre lens of the Goldmann three-mirror contact lens. When the focus was moved to the cornea, the dark ring became sharper and was noticed to originate from the inlay. In the fundus image through the Goldmann three-mirror contact lens, another dark shadow projected on the retina was observed aside of the dark ring, which moved according to the direction of the slit-light beam by shifting a slit-lamp lever and was considered to be a shadow of the inlay. The central lens of the Goldmann three-mirror lens has a flat front surface, and it had the same optical structure as the flat contact lens used for vitrectomy but without endoillumination.

The light passes through all parts of the optics of the crystalline lens or the intraocular lens (IOL) within the diameter of the pupil with the flat or prism contact lens system during vitreous surgery or a three-mirror contact lens. This is the reason why a defocused dark ring was observed in the visual field with a three-mirror contact lens. Yılmaz et al. (2011) described two cases that underwent phacoemulsification with IOL implantation with no intraoperative complications 3 and 4 years after the inlay implantation.

When vitreous surgery was performed with a flat contact lens and the focus was on the retina, the dark ring was more defocused resulting in a decrease in contrast of the retinal images. To avoid blocking the view of the retina, the eye must be rotated during vitreous surgery. Otherwise, the corneal inlay can be removed before the vitreoretinal surgery. Using a wide-angle viewing system which has a similar optical system as the indirect ophthalmoscope and fundus camera, may be recommended to increase the quality of view.

References

Casas-Llera P, Ruiz-Moreno JM Alió JL (2011): Retinal imaging after corneal inlay implantation. J Cataract Refract Surg **37**: 1729–1731.

Charman WN (2008): The eye in focus: accommodation and presbyopia. Clin Exp Optom **91**: 207–225.

Tomita M, Kanamori T, Waring GO IV, Yukawa S, Yamamoto T, Sekiya K Tsuru T (2012): Simultaneous corneal inlay implantation and laser *in situ* keratomileusis for presbyopia in patients with hyperopia, myopia, or emmetropia: six-month results. J Cataract Refract Surg **38**: 495–506.

Yilmaz OF, Bayraktar S, Agca A, Yilmaz B, McDonald MB van de Pol C (2008): Intracorneal inlay for the surgical correction of presbyopia. J Cataract Refract Surg **34**: 1921–1927.

Yılmaz OF, Alagöz N, Pekel G, Azman E, Aksoy EF, Cakır H, Bozkurt E Demirok A (2011): Intracorneal inlay to correct presbyopia: long-term results. J Cataract Refract Surg **37**: 1275–1281.

Correspondence:
Makoto Inoue, MD
Kyorin Eye Center
School of Medicine
Kyorin University
6-20-2 Shinkawa
Mitaka
Tokyo 181-8611, Japan
Tel: + 81 422 475511, ext.2606
Fax: + 81 422 469309
Email: inoue@eye-center.org

Low-Frequency Subthalamic Nucleus Stimulation in Parkinson's Disease: A Randomized Clinical Trial

Hui Ming Khoo, MD,[1] Haruhiko Kishima, MD, PhD,[1]* Koichi Hosomi, MD, PhD,[1,2] Tomoyuki Maruo, MD, PhD,[1,2] Naoki Tani, MD, PhD,[1,3] Satoru Oshino, MD, PhD,[1] Toshio Shimokawa, PhD,[4] Masaru Yokoe, MD, PhD,[2,5] Hideki Mochizuki, MD, PhD,[5] Youichi Saitoh, MD, PhD[1,2] and Toshiki Yoshimine, MD, PhD[1]

[1]*Department of Neurosurgery, Osaka University Graduate School of Medicine, Osaka, Japan* [2]*Department of Neuromodulation and Neurosurgery, Osaka University Office for University-Industry Collaboration, Osaka, Japan* [3]*Department of Neurosurgery, Otemae Hospital, Osaka, Japan* [4]*Department of Ecosocial System Engineering, Graduate School of Medicine and Engineering, University of Yamanashi, Yamanashi, Japan* [5]*Department of Neurology, Osaka University Graduate School of Medicine, Osaka, Japan*

ABSTRACT

Background: Low-frequency, bilateral stimulation of the subthalamic nucleus can improve axial symptoms of advanced Parkinson's disease (PD), but it is not particularly effective for segmental symptoms.

Methods: The optimal contacts for low-frequency (60 Hz) and high-frequency (130 Hz) single monopolar stimulation were determined. Then, in a randomized, double-blind, prospective crossover manner, 60-Hz and 130-Hz stimulations via the respective optimal contacts were compared for immediate efficacy in improving the motor function of patients with PD.

Results: The optimal contacts for 60-Hz stimulation were situated more ventrally than those for 130-Hz stimulation ($P = 0.038$). Under the respective optimal, single monopolar stimulation, 60 Hz provided superior efficacy over 130 Hz in improving the total Unified Parkinson's Disease Rating Scale motor score ($P < 0.001$) and the akinesia ($P = 0.011$) and axial motor signs ($P = 0.012$) subscores without compromising the therapeutic effect on tremor and rigidity.

Conclusions: Low-frequency stimulation via the optimal contacts is effective in improving overall motor function of patients with PD. © 2014 International Parkinson and Movement Disorder Society

Key Words: Parkinson's disease; deep brain stimulation; subthalamic nucleus; low-frequency stimulation; motor function

Subthalamic nucleus (STN) deep brain stimulation (DBS) is a well-established treatment aimed at controlling motor symptoms of Parkinson's disease (PD). Over the long term, however, axial symptoms (gait, postural stability, and speech) worsen in 60% to 80% of patients treated by STN-DBS.[1] Recent studies have suggested that STN stimulation at relatively low frequency (ie, 60-80 Hz) may be beneficial in controlling axial symptoms that continue to deteriorate under high-frequency stimulation.[2-5] However, findings regarding the effect on segmental symptoms (tremor, rigidity, and bradykinesia) have been somewhat inconsistent. Although it has been reported that the dorsal STN is the ideal target for high-frequency STN-DBS,[6,7] ventral contacts were used in the majority of patients in a study that reported satisfactory effects with low-frequency 60-Hz STN stimulation.[2] These observations prompted us to postulate that the optimal contact sites differ for high-frequency stimulation and relatively low-frequency stimulation. In a single-center, randomized, double-blind, crossover study, we tested the efficacy of relatively low-frequency stimulation via its optimal contacts for improving overall motor function of patients with PD who were treated with bilateral STN-DBS.

Patients and Methods

The study was conducted in 2 stages. Stage 1 was a double-blind study performed before randomization to determine the optimal contacts for each of the relatively low-frequency 60-Hz stimulation and the high-frequency 130-Hz stimulation. Optimal contacts were defined as single monopolar contacts that yielded the best Unified Parkinson's Disease Rating Scale motor examination (UPDRS-III) score. Stage 2 was a randomized, double-blind, crossover study to assess the immediate effects of 60-Hz and 130-Hz stimulation via the respective optimal contact sites (hereafter called *optimal-60-DBS* and *optimal-130-DBS*, respectively). Patients were randomly assigned to undergo assessments in 1 of 2 treatment sequences. In sequence A, patients were treated under optimal-130-DBS for 1 hour. After the first evaluation, the treatment condition was changed to optimal-60-DBS, and a second evaluation was conducted 1 hour later. In sequence B, the order of the treatment condition was reversed (Supporting Fig. 2). For a detailed description of the

Additional Supporting Information may be found in the online version of this article.

*Correspondence to: Dr. Haruhiko Kishima, Department of Neurosurgery, Osaka University Graduate School of Medicine, 2-2 Yamadaoka, Suita, Osaka 565-0871, Japan; hkishima@nsurg.med.osaka-u.ac.jp

Funding agencies: This study was supported by departmental resources only.

Relevant conflicts of interest/financial disclosures: Nothing to report. Full financial disclosures and author roles may be found in the online version of this article.

Received: 14 November 2012; **Revised:** 18 December 2013; **Accepted:** 18 December 2013

Published online 21 January 2014 in Wiley Online Library (wileyonlinelibrary.com). DOI: 10.1002/mds.25810

TABLE 1. Results of analysis of test scores under optimal-60-DBS and optimal-130-DBS

Outcome Measures	Maximum Possible Score[a]	Optimal-130-DBS	Optimal-60-DBS	Carry-Over Effect: *P* Value	Difference[b]	*P* Value
Primary outcome measure: Mean ± SD[c]						
UPDRS-III total score	108	16.0 ± 6.9	11.4 ± 7.2	0.603	4.6 ± 4.0	< 0.001[d]
Secondary outcome measures: Median [IQR][e]						
UPDRS-III subscores						
Axial motor signs	16	4.5 [1.5-5]	3.5 [1-4]	0.825	1 [0-1]	0.012[d]
Akinesia	32	7 [5.25-9]	7 [2-6.5]	0.153	2 [1.25-4]	0.011[d]
Tremor	28	0 [0-1]	0 [0-1]	0.368	0 [0]	1.000
Rigidity	20	2 [2-3.75]	2 [2-2.75]	0.387	0 [0-1]	0.214
Timed 10-meter walk test						
Completion time(s)	—	9.5 [8.6-10.9]	9.3 [8.5-10.3]	0.755	0.7 [0.2-1]	0.006[d]
No. of steps	—	19 [18-23]	19 [16-22]	0.755	1 [0.5-1.5]	< 0.001[d]
Freezing of gait	—	0 [0]	0 [0]	—	0 [0]	—
Berg Balance Scale[f]	56	50 [46.5-52]	51 [49-55]	0.918	1.8 [0-2.4]	0.062

[a]Higher scores on the Berg Balance Scale represent better function. Higher scores on all other items represent worse function.
[b]The differences between scores under optimal-130-DBS and optimal-60-DBS were assessed for each patient. The numbers shown are absolute values of the mean ± SD or the median [IQR].
[c]Because the UPDRS-III total scores were normally distributed according to the Shapiro-Wilk *W* test, this analysis was by *t*-test.
[d]These are statistically significant *P* values.
[e]Secondary outcome measures were analyzed using the Mann-Whitney *U* test.
[f]Because 1 patient did not complete the Berg Balance Scale assessment, the analysis was based on data from 13 patients.
Abbreviations: Optimal-130-DBS, 130-Hz (high-frequency) deep brain stimulation at the optimal contact site; Optimal-60-DBS, 60-Hz (low-frequency) deep brain stimulation at the optimal contact site; SD, standard deviation; UPDRS, Unified Parkinson's Disease Rating Scale; IQR, interquartile range.

study protocol, including the method of active contacts optimization, see the Supporting Information and Supporting Figures 1 and 2.

The study was conducted with patients taking their usual antiparkinsonian medications. To minimize symptom fluctuation due to medication, each assessment session started at least 1.5 hours after administration of the usual levodopa dose and ended before the next dose (Supporting Fig. 2).[8,9] Each session lasted approximately 3 hours and was conducted in a single morning or afternoon to minimize circadian fluctuation. The off-medication state was not assessed for the patients' safety and comfort.

Study recruits were independent, ambulating patients with advanced PD who were treated with bilateral STN-DBS. For details of the inclusion criteria, see the Supporting Information. The Ethics Committee of Osaka University Hospital approved the protocol (approval no. 11256). All study patients provided written informed consent for their participation.

The primary outcome measure was the difference in total UPDRS-III score between the two stimulation conditions. Secondary outcome measures were UPDRS-III subscores, gait evaluated by means of the 10-meter timed walk test at preferred pace,[10] and postural stability evaluated by the Berg Balance Scale (BBS).[11] See Supporting Information for details of the outcome measures, assessments, and statistical analysis, according to the Consolidated Standards of Reporting Trials (CONSORT) guidelines.

Results

Sixteen patients were assessed for eligibility. One patient did not meet the inclusion criteria, and 1 patient who withdrew during the first stage 1 session was reluctant to participate in the 3-hour assessment. The remaining 14 patients were randomized and completed the study (Supporting Fig. 1). Patient characteristics and DBS settings are summarized in Supporting Tables 1 and 2, respectively.

Stage 1: Optimal Contacts for 60-Hz and 130-Hz Stimulations

Group analysis revealed a significant difference in the optimal contact positions between 60-Hz and 130-Hz stimulations ($P = 0.038$), with the optimal contacts for 60-Hz stimulation being more ventrally distributed (Supporting Fig. 3A,B). Individual analyses revealed that the optimal contact positions varied with respect to stimulation frequency in 5 of the 14 patients (Supporting Fig. 3C,D). Optimal contacts for 130-Hz and 60-Hz stimulations are shown for each patient in Supporting Table 3.

Stage 2: Immediate Effects of Optimal-60-DBS

Optimal-60-DBS yielded a mean UPDRS-III score of 4.6 points (standard deviation, 4.0 points) less than that of optimal-130-DBS ($P < 0.001$). No significant carry-over effect ($P = 0.603$) confounded the treatment effect (Table 1).

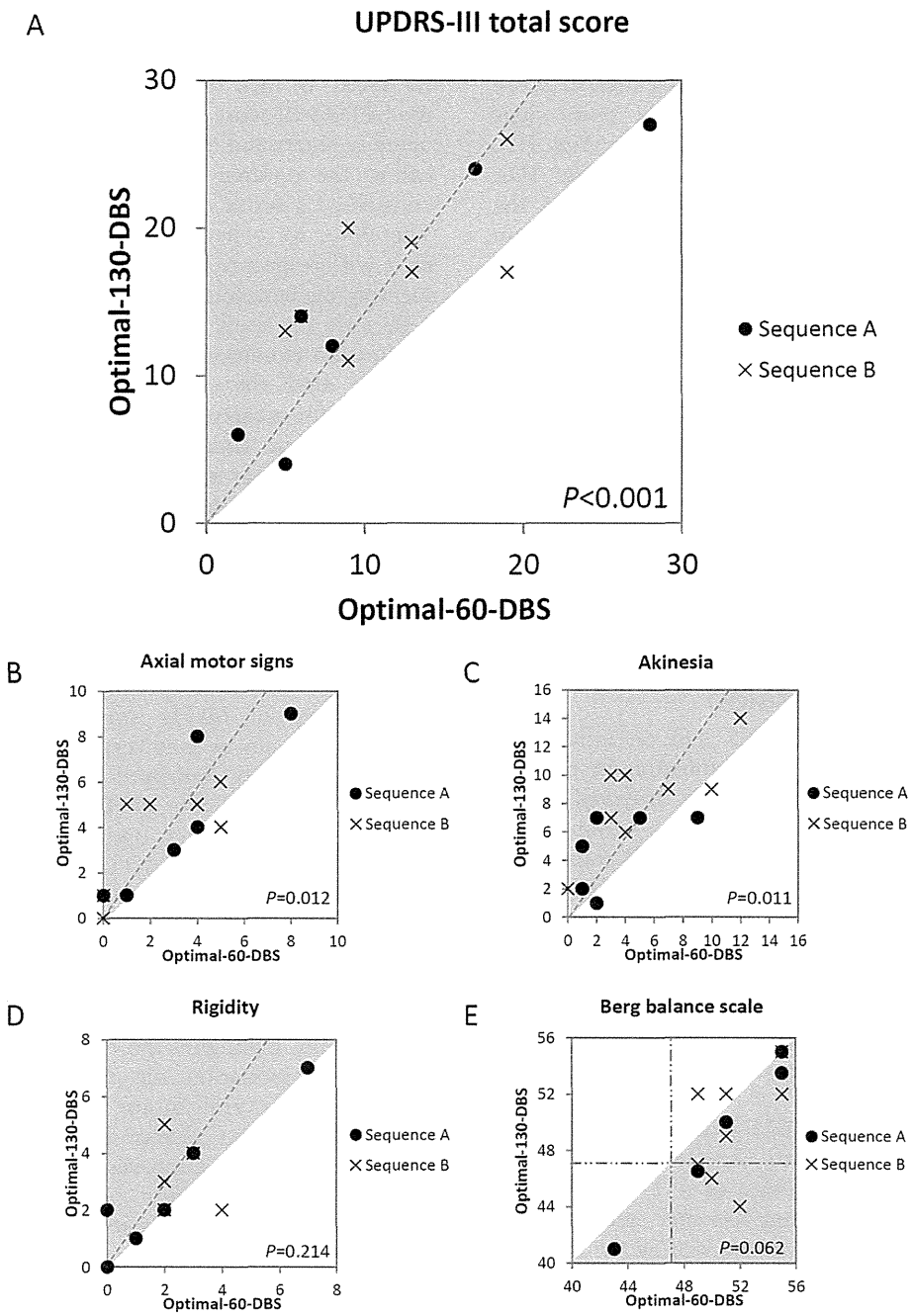

FIG. 1. (**A-E**) These scatter plots illustrate scores under 60-Hz and 130-Hz stimulation via the respective optimal contacts ("optimal-60-DBS" and "optimal-130-DBS", respectively). In **A** through **D**, the dashed lines correspond to the 30% score reductions produced by optimal-60-DBS. In **E**, the dashed-and-dotted lines correspond to the cutoff score of 47 for identifying patients who were at risk of falling.[12]

With respect to UPDRS-III subscores, optimal-60-DBS, compared with optimal-130-DBS, yielded significantly less severe axial motor signs ($P = 0.012$) and akinesia scores ($P = 0.011$). However, no significant difference between the 2 DBS conditions was observed in tremor ($P = 1.000$) or rigidity ($P = 0.214$) (Table 1). Optimal-60-DBS resulted in statistically significant less time ($P = 0.006$) and fewer steps ($P < 0.001$) needed to complete the 10-meter walk. No freezing of gait was observed under either DBS condition (Table 1), although most patients exhibited freezing of gait in the OFF-DBS condition. The BBS score tended to be higher under optimal-60-DBS ($P = 0.062$).

On an individual level, a good response (≥30% score reduction) to optimal-60-DBS was observed in 7 of the 14 patients in terms of total UPDRS-III score (Fig. 1A), in 5 patients in terms of axial motor signs (Fig. 1B), in 8 patients in terms of akinesia (Fig. 1C), but in only 3 patients in terms of rigidity (Fig. 1D). Slight tremor was observed in 5 patients, but the tremor subscores did not vary with the stimulation conditions (data not shown). Patients with PD who had a BBS score <47 reportedly are at risk of falling.[12] In our patient series, optimal-60-DBS, versus optimal-130-DBS, tended to result in fewer patients at risk of falling (Fig. 1E). Stimulation settings are shown for each patient in Supporting Table 3.

Adverse Effects

No serious or prolonged adverse effects attributed to the adjustment of stimulation settings were seen. Adjustment was frequently associated with transient paresthesia and mild dyskinesia in stage 1 (Supporting Table 4). No adverse effects were reported in stage 2.

Discussion

In this study, optimal-60-DBS had an immediate, positive effect on overall motor function in patients with PD. The 4.6-point improvement observed in this study is clinically important, because the minimal clinically important change in the UPDRS-III total score ranges from 2.3 to 5.0.[13,14] In terms of UPDRS-III subscores, optimal-60-DBS was better for controlling axial symptoms and akinesia and was equally as effective as optimal-130-DBS for controlling rigidity and tremor. On an individual level, optimal-60-DBS was more effective in improving total motor function in half of the patients and was comparable to optimal-130-DBS in the other half.

Optimal-60-DBS significantly reduced the time and number of steps required to complete the 10-meter walk. However, the importance of a 1-step/10-meter reduction and a 0.7-second/10-meter reduction is undetermined, because data substantiating the minimal clinically important change in these measures are lacking for PD patients.[15] Considering that most patients reported ease of walking during assessments under optimal-60-DBS (data not shown), we concluded that these relatively small differences are potentially substantial to improve gait in these patients. Although optimal-60-DBS was not superior for improving postural stability, it is potentially beneficial for reducing the risk of falling in patients with advanced PD.

Another important result is the difference in optimal contacts between 60-Hz and 130-Hz stimulations. The difference was observed in 36% of the patients, and the optimal contacts for 60-Hz stimulation were always relatively ventral whenever the difference in optimal contacts between frequencies was observed. This is interesting and worth further study, because the dorsolateral STN has long been recognized as the ideal target for DBS.[7] In fact, optimal-60-DBS similarly improved the UPDRS-III score in patients with more ventrally situated contacts and in patients with contact sites identical to the optimal-130-DBS contact sites. This was considered a result of the active contact optimization. Therefore, we believe that optimizing the active contacts with respect to frequency is very important in augmenting the beneficial effect of 60-Hz stimulation.

Because the study was not conducted under the off-medication condition and assessments were performed 1 hour after the change in stimulation, there was potential for a carry-over effect arising from the medication or first stimulation. However, the crossover design allowed for an analysis of any carry-over effect, which would manifest as a difference in the baseline measures within the time interval between the first and the second stimulations; no significant carry-over effect was found (Table 1). Thus, neither the timing of assessments relative to that of drug administration nor the short-term nature of the observations critically affected our results. Our study showed only the immediate effects of 60-Hz stimulation via the single monopolar contacts. It is very common for patients to have a transiently improved response to a change in stimulation. Despite the small sample size, which was another study limitation, optimal-60-DBS led to a significant improvement in the therapeutic effect of STN-DBS on motor symptoms. Overall, it will be important to test the long-term effects in controlled trials incorporating large numbers of patients and to test the effects using stimulation with more complex configurations, such as bipolar, tripolar, or multiple cathodes.

This study highlights the efficacy of relatively low-frequency stimulation via the optimal contacts in improving the overall motor function of patients with advanced PD who receive bilateral STN-DBS. This stimulation strategy improves axial symptoms without compromising the effect on segmental symptoms. Thus, the strategy is a potential option for patients who suffer axial symptoms despite successful STN-DBS. ■

References

1. Merola A, Zibetti M, Angrisano S, et al. Parkinson's disease progression at 30 years: a study of subthalamic deep brain-stimulated patients. Brain 2011;134:2074-2084.
2. Moreau C, Defebvre L, Destee A, et al. STN-DBS frequency effects on freezing of gait in advanced Parkinson disease. Neurology 2008;71:80-84.
3. Moreau C, Pennel-Ployart O, Pinto S, et al. Modulation of dysarthropneumophonia by low-frequency STN DBS in advanced Parkinson's disease. Mov Disord 2011;26:659-663.
4. Ricchi V, Zibetti M, Angrisano S, et al. Transient effects of 80 Hz stimulation on gait in STN DBS treated PD patients: a 15 months follow-up study. Brain Stimul 2012;5:388-392.

5. Brozova H, Barnaure I, Alterman RL, Tagliati M. STN-DBS frequency effects on freezing of gait in advanced Parkinson disease [letter]. Neurology 2009;72:770; author reply 770-771.
6. Benarroch EE. Subthalamic nucleus and its connections: anatomic substrate for the network effects of deep brain stimulation. Neurology 2008;70:1991-1995.
7. Aravamuthan BR, Muthusamy KA, Stein JF, Aziz TZ, Johansen-Berg H. Topography of cortical and subcortical connections of the human pedunculopontine and subthalamic nuclei. Neuroimage 2007;37:694-705.
8. Moore ST, MacDougall HG, Gracies JM, Ondo WG. Locomotor response to levodopa in fluctuating Parkinson's disease. Exp Brain Res 2008;184:469-478.
9. Adamiak U, Kaldonska M, Klodowska-Duda G, et al. Pharmacokinetic-pharmacodynamic modeling of levodopa in patients with advanced Parkinson disease. Clin Neuropharmacol 2010;33:135-141.
10. Miyai I, Fujimoto Y, Ueda Y, et al. Treadmill training with body weight support: its effect on Parkinson's disease. Arch Phys Med Rehabil 2000;81:849-852.
11. Qutubuddin AA, Pegg PO, Cifu DX, Brown R, McNamee S, Carne W. Validating the Berg Balance Scale for patients with Parkinson's disease: a key to rehabilitation evaluation. Arch Phys Med Rehabil 2005;86:789-792.
12. Leddy AL, Crowner BE, Earhart GM. Functional gait assessment and balance evaluation system test: reliability, validity, sensitivity, and specificity for identifying individuals with Parkinson disease who fall. Phys Ther 2011;91:102-113.
13. Shulman LM, Gruber-Baldini AL, Anderson KE, Fishman PS, Reich SG, Weiner WJ. The clinically important difference on the Unified Parkinson's Disease Rating Scale. Arch Neurol 2010;67:64-70.
14. Schrag A, Sampaio C, Counsell N, Poewe W. Minimal clinically important change on the Unified Parkinson's Disease Rating Scale. Mov Disord 2006;21:1200-1207.
15. Tomlinson CL, Patel S, Meek C, et al. Physiotherapy versus placebo or no intervention in Parkinson's disease [serial online]. Cochrane Database Syst Rev 2012;(8):CD002817.

Patient-specific Contour-fitting Sheet Electrodes for Electrocorticographic Brain Machine Interfaces

Masayuki Hirata, Shayne Morris, Hisato Sugata, Kojiro Matsushita, Takufumi Yanagisawa, Haruhiko Kishima, and Toshiki Yoshimine

Abstract—**Non-invasive localization of certain brain functions may be mapped on a millimeter level. However, the inter-electrode spacing of common clinical brain surface electrodes still remains around 10 mm, and some electrodes fail to measure cortical activity due to unconformable plain electrode sheets. Here, we present details on development of implantable electrodes for attaining higher quality electrocorticographic signals for use in functional brain mapping and brain-machine interfaces. We produced personalized sheet electrodes after the creation of individualized molds using a 3D-printer. We created arrays to fit the surface curvature of the brain and inside the central sulcus, with inter-electrode distances of 2.5 mm. Rat experiments undertaken indicated no long term toxicity. We were also able to custom design, rapidly manufacture, safely implant and confirm the efficacy of personalized electrodes, including the capability to attain meaningful high gamma-band information in an amyotrophic lateral sclerosis patient. This sheet electrode may contribute to the higher performance of BMI's.**

I. Introduction

Recent developments in the area of brain machine interfaces (BMIs) have led to the possibility of a seamless interface between the human brain and devices [1]. To achieve this, neural signals must decoded to interpret their meaning, where decoding relies on the quality of the measured neural signals, particularly those of the high gamma-band range (60 – 200 Hz).

One practical method for obtaining high quality neural activity is intracranial electrodes. Brain surface electrodes or electrocorticographic (ECoG) electrodes are less invasive because they do not penetrate the brain tissue. We have shown that intra-sulcal ECoG electrodes on the motor side of the central sulcus provided a higher performance than those of the gyral ECoG [2].

Research supported in part by "Brain Machine Interface Development" and "Development of BMI Technologies for Clinical Application" under the Strategic Research Program for Brain Sciences by the Ministry of Education, Culture, Sports, Science and Technology (MEXT) Japan, by KAKENHI (22390275, 23390347) by Japan Society for the Promotion of Science (JSPS), and by Health Labour Sciences Research Grant (23100101) by the Ministry of Health Labour and Welfare.

Masayuki Hirata is with Osaka University Medical School, 2-2 Yamadaoka, Suita, Osaka, 565-0871 JAPAN (corresponding author to provide phone: +81-6-6210-8429; fax: +81-6-6210-8430; e-mail: mhirata @nsurg.med.osaka-u.ac.jp).

Morris Shayne, Hisato Sugata, Kojiro Matsushita, Takufumi Yanagisawa, Haruhiko Kishima, and Toshiki Yoshimine are also with Osaka University Medical School, (e-mail: shayne.morris@gmail.com, {hsugata|matsushita|yanagisawa|hkishima|yoshimine}@nsurg.med.osaka-u.ac.jp).

However, the inter-electrode spacing of standard clinical ECoG electrodes still remains at about 10mm. In addition, the gyral and sulcal surface of the human brain is curved with bumps, depressions and grooves, called gyri and sulci, thus making a one-fits-all approach to the design of electrodes, which has been the mainstay until now, inefficient. Actually, standard clinical ECoG electrodes often fail to measure cortical activity due to unconformable plain electrode sheets.

With these in mind, we aimed to create a high density array of electrodes designed to match the contour of an individual's brain surface as well as to place electrodes both on the gyral surface, and inside the central sulcus. In this article, we also describe the placement of patient-specific cortical electrodes into an ALS patient.

II. Methods

A. Electrode Sheets

1) *Sulcal Electrode Sheet*: We individualized the shape of the sheet containing the electrodes using a press mold system. Our method sandwiches the electrodes in-between silicone sheets individualized to fit the surface of an individual patient's brain.

Informed consent was obtained from healthy volunteers and patients, after authorization from the medical ethics committee of our institution. First we took a 1 mm thin-slice MRI series of the subject's brain. We then imported the MRI data into BrainVISA 4.0.2 (http://brainvisa.info/), where we ran the sulci extraction routine which allowed us to generate a 3D image of the brain surface, and also exudate the majority of the sulci (Fig. 1A). The 3D data of the central sulcus were then imported into two 3D computer aided designing (CAD) software (Mimics v14.12, 3-matic v5.1, Materialise N.V. Leuven Belgium). The surface data of the motor side was selected for further processing with 3-matic.

Next, sides were extended downward from the surfaces, after which, a base was then added to generate CAD data for a mold of the central sulcus. Then an inverse of this mold was produced, so that we now had both male and female molds. Holes were placed in the four corners of the base of the molds to allow for adjustments of the thickness of the silicon electrode sheets (Fig. 1A).

Using this data, we then used a 3D printer (Polyjet 3D printer, Objet Geometries Ltd., Israel) to create the actual molds (Fig. 1B). We marked the desired positions of the electrodes on the mold surface, with the surface facing the motor bank of the central sulcus having 35 electrodes while

978-1-4244-7929-0/14/$26.00 ©2014 IEEE

the surface facing the sensory bank had 15, since the primary motor cortex provides greater information on motor function. We also placed a higher emphasis on the hand-knob area in the form of higher electrode densities.

A silicone sheet (SILASTIC MDX4-4210) was then heated and placed on the mold. The silicone sheet was then carefully removed from the molds after cooling naturally to room temperature. The same process was repeated to produce 3 sheets; motor side, sensory side, and intermediate between these two. Next, holes were punched out for the electrodes at predetermined locations. Platinum electrodes were in-set into these locations. Flexible stainless leads (diameter 0.05 mm polyurethane coated, impedance $\leq 80\Omega$) were attached individually to each of the electrodes (impedance: electrodes $\leq 10\Omega$, lead ends (platinum) $\leq 10\Omega$). The lead wires passed through a silicone tube. To fix the electrodes, wires, and silicone tube, a silicone adhesive was added and the second silicone sheet placed on top and compressed in the mold (Fig. 1B). The process was repeated for the sensory side electrodes, the end result being 2 sets of plate electrodes sandwiched between 3 silicone sheets (Fig. 1C).

2) *Gyral Electrode Sheet*: Using the same process, we also created patient-specific gyral electrodes. These sheets were designed to have electrodes on only the side facing the cortical surface, and the locations and densities of the electrodes were tailored to match the functional areas of this surface. Next, the same 3D printing methods were used to create a model of the subject's brain to confirm that the manufactured electrodes fitted properly into the central sulcus, and onto the surface of the brain.

B. Strength, Cytotoxicity and Biocompatibility Tests

In order to test the safety of the electrodes before implantation into patients, we undertook the following tests.

1) *Physical Tests*: Prior to clinical trials, to test the strength of the sheet electrodes, a 3 dimensional sheet electrode (10 mm x 60 mm silicone electrode sheet with 50 mm x 1.3 mm diameter lead) was prepared and underwent dynamic tensile and compression tests (TENSILON RTF1250 (A&D), Gauge length 25 mm, stretching speed 500 mm/min, load cell 1kN, 10kN, 22°C 57% humidity).

2) *Cytotoxicity Tests*: Cytotoxicity tests were undertaken with concern to the effects of 3D-high density electrode extract on Chinese hamster fibroblasts (JCRB0603:V79) in accordance with the ISO 10993-5: 2009(E) Biological evaluation of medical devices - Part 5: Tests for in vitro cytotoxicity, ISO 10993-12: 2007 (E) Biological evaluation of medical devices - Part 12 : Sample preparation and reference materials standards, and other related Japanese protocols. In these tests, the sheet electrodes were broken down into 2 x 15 mm sections containing all the constituents of the electrodes. Ten mL of medium per 1g of morcellation was added to these sections and then, sealed, shielded from light, and cultivated with the Chinese hamster fibroblasts (JCRB0603:V79) for 24 hours. As positive controls, polyurethane films containing 0.1% and 0.25% zinc diethyldithiocarbamate (referred to respectively, as positive control A and B respectively) were used, while a high density polyurethane film was used as a negative control.

3) *Biocompatibility Tests*: 3D-high density electrodes and control materials (diameter 20 mm) were implanted subcutaneously into 12 male rats and then removed after 26 weeks to examine the effects of the subject material on the implanted rats. The electrodes and a control material were symmetrically implanted subcutaneously at the dorsal end of the spinal column while the subject was under intraperitonial anesthesia, with the electrodes implanted on the left side and the control (high density polyethylene sheet (1 mm x 50 mm x 100 mm) implanted on the right side of the scapula.

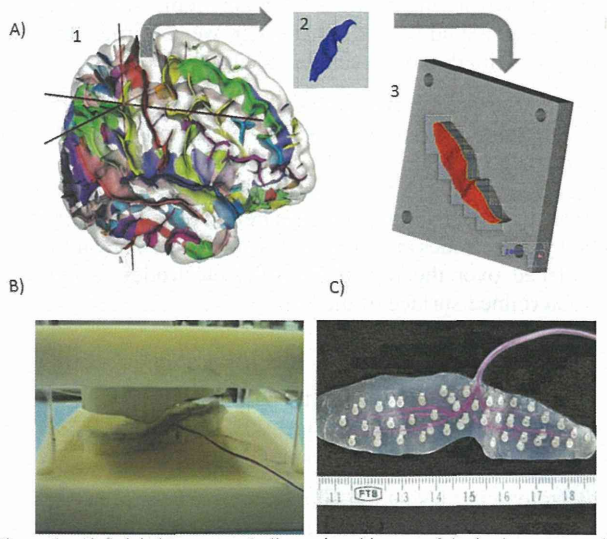

Figure 1. A) Sulci shown on a 3-dimensional image of the brain, generated with BrainVISA® from a subjects MRI data. CAD data of a mold created from the surface of the central sulcus was created with 3-matic®. B) Silicone sheet compression between male and female molds created with a 3D printer. C) A silicone sheet is created on the mold, and holes were made for electrode embedding. Flexible stainless leads were then connected.

C. Clinical Test

We designed 3D personalized electrodes for temporary implantation into an Amyotrophic lateral sclerosis (ALS) patient, as part of our clinical brain machine interface trial on severe ALS patients. The patient was a 61 year old male, who was only able to communicate using eye movement and a letter chart, or using an assistive communication device by a switch triggered by minute movements of the patient's lips. He had a total quadra-paralysis and was in a locked-in state. Informed consent was obtained. The trial was thoroughly reviewed and authorized by the medical ethics committee of our institution. Pre-operative magnetoencephalography (MEG) were undertaken to test the suitability of the patient, prior to electrode implantation.

IV. Results

A. Electrode Sheets

1) Central Sulcus Electrode Sheet: We were able to manufacture an array of electrodes with an inter-electrode distance between electrodes of 2.5 mm (a density of 16 times that of previous standard types), and we were able to create

sheet electrodes molded to fit inside the central sulcus with a total of 50 plate electrodes (35 facing the motor bank and 15 facing the sensory bank). The length of the central sulcus electrode shown is around 95 mm x 24 mm. Unlike the standard-type electrodes that we have previously placed within the central sulcus at our institution which were strip electrodes (4 x 1 electrodes) in one dimension, our patient-specific sheet electrode was 2 dimensional (11~17 x 2~3 electrodes). Distances from the surface of the sheet electrode to the mold were 2.2 mm and 0.1 mm at maximum length extremities, and 3.8 mm and 1.2 mm at maximum width extremities, with an average distance of 1.8±1.4 mm (mean±SD). The thickness varied between 0.81 ~ 0.96 mm at sampled locations. Using a 3D model of the same subject's brain, also created with the 3D printer, we confirmed that the electrodes fitted into the central sulcus.

2) Gyral Surface Electrode Sheet: The sheet shown here has 70 electrodes, which are located at various densities in accordance with anatomically perceived functionality, such as the hand-knob. As well as matching the contour of the patient's cortical surface, the sheet electrodes are softer than standard electrodes and are thus less invasive. They may also be placed over the top of the sulci electrodes to cover a predetermined surface of the brain.

B. Strength, Cytotoxicity and Biocompatibility Tests

1) Physical Tests: The electrodes passed the set strength level (silicone sheet 5N, leads 50N) tests with values of 9.58N for the silicone sheet, and more than 60N for the leads.

2) Cytotoxicity: Using the 100% negative control extract we confirmed that the number of colonies were almost unchanged. The IC50s for Positive Control A and B were 0.91% and 57.0% respectively. The IC50 for the positive control was 2.31μg/mL, thus indicating no strong cytotoxicity on colony growth.

3) Biocompatibility: One out of 12 rats showed slight swelling at the sites of implantation four days after sub-cutaneous placement. In this subject, swelling on the electrode implanted side continued for 41 days, while swelling on the control implanted side was also observed for 19 days. Superficial abnormalities disappeared after 20 days on the control implanted side and 42 days on the electrode implanted side but reoccurred on the electrode implanted side 175 days after implantation. Examinations after the completion of the test period indicated the presence of an abscess most likely due to infection at the time of implantation. None of the other 11 subjects developed abnormalities over the test period.

C. Clinical Test

In this clinical test, we designed only gyral electrodes. After the creation of gyral molds using our patient-specific method described previously (Fig. 2A), sheet electrodes were manufactured targeting mainly the primary motor cortex; 53 plate electrodes over the primary motor cortex with a higher density over the hand knob, 17 over the premotor cortex, and 24 over the somatosensory cortex (Fig. 2B). We used a neuronavigational system for presurgical planning and intraoperative navigation to determine the optimal site for craniotomy. Intraoperatively, we performed craniotomy at the pre-determined site, and identified the pre-operative anatomical features of the cortical surface (pre-central gyrus, and cortical veins etc.). We also reconfirmed the location of the central sulcus through N20 phase reversal of somatosensory evoked potentials. The sheet electrode was placed subdurally based on these pre-operative and intra-operative findings. The electrodes closely fitted the contour of the brain surface as was designed (Fig. 2C). Postoperatively, EEG monitoring showed that clear ECoG signals were obtained from all electrodes (Fig. 2D). Notably, localized high gamma band activity induced by motor imaginary tasks were clearly detected by the electrodes located over the hand-knob area (Fig. 3). During the clinical test, real time control of a robotic arm was also evaluated (not shown in this paper). The electrodes were removed as scheduled 21 days after implantation without any further deterioration in neurological symptoms.

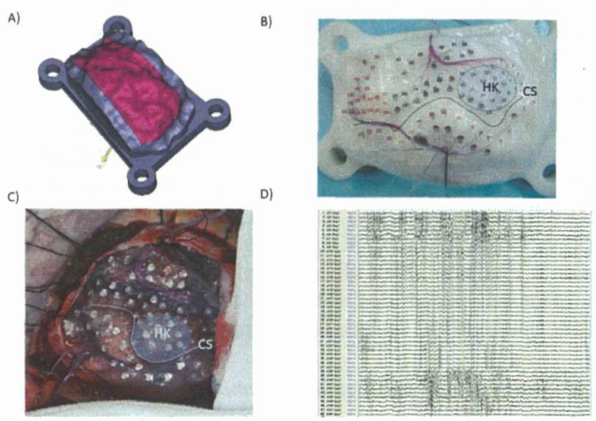

Figure 2. A) CAD model of ALS patient's brain surface covering S1, M1 and the pre-central gyri indicated in pink. B) Completed sheet electrodes placed on a brain surface model. CS indicates the central sulcus, and HK indicates the hand knob. C) Intra-operative image after placement of electrodes, with the white dotted line indicating the central sulcus and the hand knob area indicated in blue. D) EEG monitoring confirming signals attained from all electrodes.

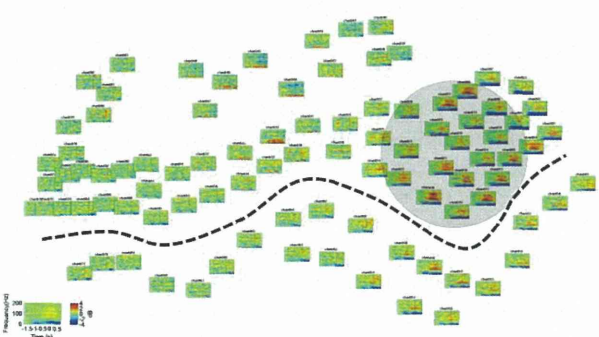

Figure 3. High gamma band activity on the cortical surface surrounding the central sulcus. Imaginary hand movement produces increased high gamma band activity in the areas surrounding the hand knob (shaded area).

V. Discussion

In the present study, by using semi-automated methods to map sulci and by utilizing CAD software and 3D printers, we were able to rapidly design and manufacture patient-specific cortical sheet electrodes with high spatial resolution for not only gyral but also sulcal implantation.

We obtained high quality signals from every electrode, including high frequency information after temporary implantation into an ALS patient.

Using our method, we were able to manufacture a sheet electrode array for placement into the central sulcus. Due to its patient-specific design, the electrode is less invasive than the standard sheet electrodes. Electrode locations can also be altered to provide higher densities within the central sulcus over areas such as the hand knob, and can be placed over the whole length of the central sulcus. Our electrodes also allow for electrodes to be placed in the direction of the motor bank, as well as the somatosensory bank, which may provide the opportunity for the sensory feedback required in close-loop systems [3].

Using the above method, we were also able to manufacture a sheet electrode for placement over the gyral surface. These sheet electrodes are patient specific and designed to match the individual surfaces of a patient's brain, thus meaning they apply less pressure at localized areas of contact than the previous types of flat 2-dimensional sheet electrodes, because all of the electrodes are in contact with the brain surface. This also means that compared to flat electrode sheets, there is a greater chance of attaining useful EEG from all electrodes.

It is also possible to increase the density of electrodes over cortical areas of higher importance, for example the hand knob. In our ALS patient trial, readable signals were obtained from all plate electrodes on the implanted sheet. It is noteworthy that we were successfully able to gain gamma-band information from specific functional areas such as the hand knob. Our high density electrodes successfully detected a variety of gamma band activities that differed from electrode to electrode despite electrodes being in close proximity (approximately 3 mm inter-electrode spacing) to one another.

The power of high gamma-band information is weak and it is difficult measure this range using standard forms of scalp EEG or MEG. On the other hand we have previously shown that gamma-band activity is useful for predicting motor activity using standard sized cortical electrodes [4], [5]. Using the high-density patient-specific cortical electrodes described in this study, we were able to measure gamma-band activity with high spatial resolution even in an ALS patient with complete paralysis.

Regarding safety, we have successfully completed the non-clinical studies necessary to move on to clinical trials, including those related to physical strength, cytotoxicity, and biocompatibility, as well as long term stability. In our ALS patient clinical trial we implanted our sheet electrode for 21 days, with no new neurological symptoms incurred after electrode removal. We will continue clinical evaluations to confirm the safety and efficacy of these sheet electrodes, moving towards the implantation of a fully-implantable wireless system [6].

VI. Conclusion

We developed a high-density patient-specific sheet electrode that fit within the sulci or on gyral surfaces. They are designed and rapidly manufactured with semi-automatic methods involving the use of a 3D-printer and resulted in the effective attainment of ECoG signals. We temporarily placed this patient-specific sheet electrode into an ALS patient and were able to attain readable signals from all plate electrodes and measured localized high gamma band activity in the hand knob area. We believe that this sheet electrode will contribute to higher performance BMI systems.

Acknowledgment

The authors wish to thank Annuar Khairul of Materialize Japan Co. Ltd for his help in the manufacturing of the models and casts using the 3D printer. We also wish to thank Shinichi Morikawa of Unique Medical Co. Ltd. for his help in the manufacturing process of the sheet electrodes.

References

[1] M. A. Lebedev and M. A. L. Nicolelis, "Brain-machine interfaces: past, present and future," Trends Neurosci., vol. 29, no. 9, pp. 536–546, 2006.

[2] T. Yanagisawa, M. Hirata, Y. Saitoh, A. Kato, D. Shibuya, Y. Kamitani, and T. Yoshimine, "Neural decoding using gyral and intrasulcal electrocorticograms," Neuroimage, vol. 45, no. 4, pp. 1099–106, May 2009.

[3] Z. Li, J. E. O'Doherty, M. A. Lebedev, and M. A. L. Nicolelis, "Adaptive decoding for brain-machine interfaces through Bayesian parameter updates," Neural Comput, vol. 23, no. 12, pp. 3162–204, Dec. 2011.

[4] T. Yanagisawa, M. Hirata, Y. Saitoh, T. Goto, H. Kishima, R. Fukuma, H. Yokoi, Y. Kamitani, and T. Yoshimine, "Real-time control of a prosthetic hand using human electrocorticography signals," J. Neurosurg., vol. 114, no. 6, pp. 1–8, Feb. 2011.

[5] T. Yanagisawa, M. Hirata, Y. Saitoh, H. Kishima, K. Matsushita, T. Goto, R. Fukuma, H. Yokoi, Y. Kamitani, and T. Yoshimine, "Electrocorticographic control of a prosthetic arm in paralyzed patients," Ann. Neurol., vol. 71, no. 3, pp. 353–61, Mar. 2012.

[6] M. Hirata, K. Matsushita, T. Suzuki, T. Yoshida, F. Sato, S. Morris, T. Yanagisawa, T. Goto, M. Kawato, and T. Yoshimine, "A Fully-Implantable Wireless System for Human Brain-Machine Interfaces Using Brain Surface Electrodes: W-HERBS," IEICE Trans. Commun., vol. E94-B, no. 9, pp. 2448–2453, 2011.

SCIENTIFIC REPORTS

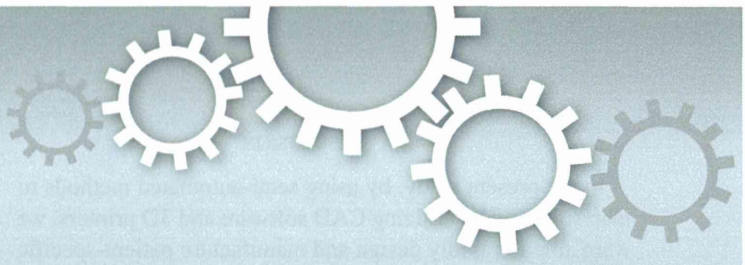

OPEN

SUBJECT AREAS:
HUMAN BEHAVIOUR
SACCADES
ATTENTION

Received
10 September 2014

Accepted
3 December 2014

Published
19 January 2015

Correspondence and requests for materials should be addressed to S.K. (kitazawa@fbs.osaka-u.ac.jp)

A model of face selection in viewing video stories

Yuki Suda[1] & Shigeru Kitazawa[1,2,3,4]

[1]Department of Neurophysiology, Graduate School of Medicine, Juntendo University, Bunkyo, Tokyo, 113-8421, JAPAN, [2]Dynamic Brain Network Laboratory, Graduate School of Frontier Biosciences, Osaka University, Suita, Osaka, 565-0871, JAPAN, [3]Department of Brain Physiology, Graduate School of Medicine, Osaka University, Suita, Osaka, 565-0871, JAPAN, [4]Center for Information and Neural Networks (CiNet), National Institute of Information and Communications Technology, and Osaka University, Suita, Osaka, 565-0871, JAPAN.

When typical adults watch TV programs, they show surprisingly stereo-typed gaze behaviours, as indicated by the almost simultaneous shifts of their gazes from one face to another. However, a standard saliency model based on low-level physical features alone failed to explain such typical gaze behaviours. To find rules that explain the typical gaze behaviours, we examined temporo-spatial gaze patterns in adults while they viewed video clips with human characters that were played with or without sound, and in the forward or reverse direction. We here show the following: 1) the "peak" face scanpath, which followed the face that attracted the largest number of views but ignored other objects in the scene, still retained the key features of actual scanpaths, 2) gaze behaviours remained unchanged whether the sound was provided or not, 3) the gaze behaviours were sensitive to time reversal, and 4) nearly 60% of the variance of gaze behaviours was explained by the face saliency that was defined as a function of its size, novelty, head movements, and mouth movements. These results suggest that humans share a face-oriented network that integrates several visual features of multiple faces, and directs our eyes to the most salient face at each moment.

When typical adults watch TV programs or movie scenes, they show surprisingly stereo-typed gaze behaviours in time and space[1–3], as typically indicated by almost simultaneous shifts of their gazes from one face to another[4]. Recent studies have shown with the aid of multidimensional scaling that such typical temporo-spatial gaze behaviours were not shared by adults with autism[4] or by monkeys[3] and were quite different from those generated artificially based on low-level physical features[3]. These previous findings suggest that temporo-spatial gaze behaviours of typical adults are driven by some human specific social "saliency", which must be different from the standard saliency model that depends solely on the low-level physical features[5,6]. In the present study, we propose a rule that determines the dynamic choice among the faces while viewing motion pictures.

First, we placed a face detection mechanism along a cascade of other factors in our model for face selection (Figure 1a) because typical adults spend most of their time viewing a face, whether they viewed motion pictures[4,7,8] or still pictures[9,10]. However, we also looked at other items in a scene; for example, text typically attracts attention[4,9,11]. Thus, in the first part of this study, we tested whether the essence of actual gaze behaviours was retained after disregarding non-face objects while they viewed short video clips that featured two or more human characters.

We then examined gaze patterns when the video clips were played without sound, to evaluate if verbal semantics plays a critical role in determining our gaze behaviour. If verbal semantics in conversation is critical, our stereo-typed gaze behaviours should be significantly altered by not providing sound. We also presented the video clips in reverse, to further test whether the normal context other than the verbal semantics is critical for the generation of gaze behaviours. If the gaze behaviours are depending solely on the low-level physical features, the behaviours should be symmetric in time reversal.

We then hypothesized that the saliency of each face is determined by a combination of its size, novelty, head movement, and mouth movement (Figure 1a). We chose size because a recent neuroimaging study has shown that responses in the fusiform face area were clearly modulated by the size of the face stimuli[12]. We added the novelty component because the amygdala, which is assumed to be a member of face detection circuits, is reported to respond strongly to novel faces[13–15]. We chose head and mouth movements because a number of face areas over the occipitotemporal cortex are responsive both to biological motion and face

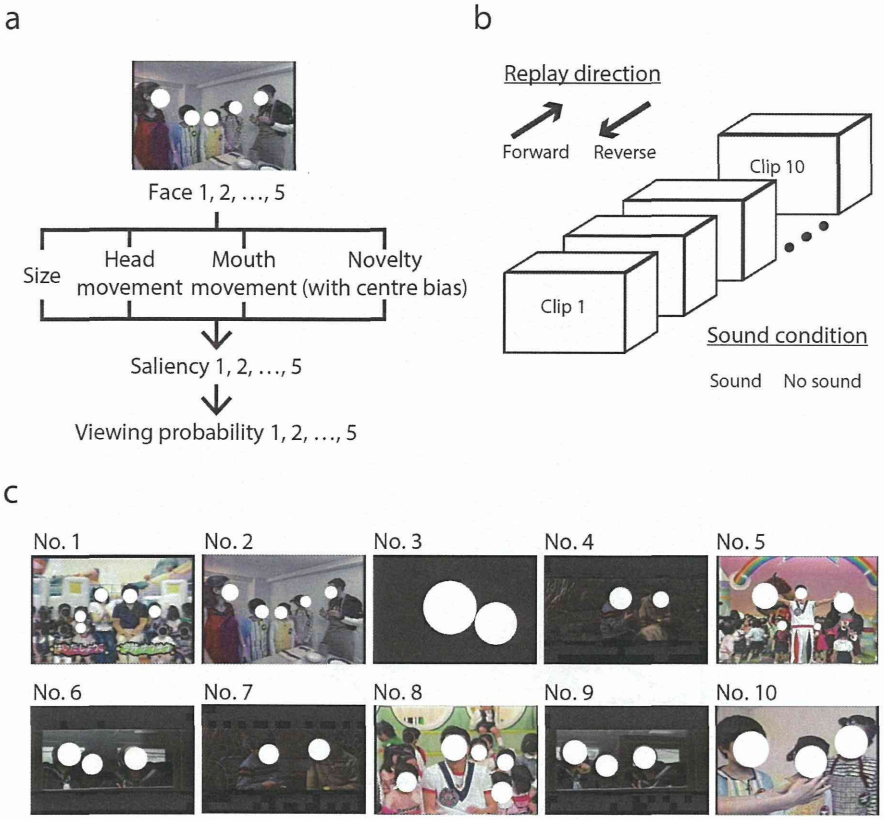

Figure 1 | Designs of the model and experiments. (a) A schematic diagram of the face saliency model. Faces were detected first, and a saliency was assigned to each as a combination of its size, head motion, mouth movement (for speech) and novelty (weighted by the distance from the screen centre). Then, the face saliency was used to predict the viewing probability of each face. (b) Replay conditions. The video stimuli (77 s long) were replayed in four different conditions in a two-by-two factorial manner: replay direction (forward/reverse) by sound condition (on/off). (c) Example frames taken from 10 video clips used for analysis. Up to five faces (circled) were chosen for calculating the viewing proportions. The other faces are covered by black circles. Note that faces were not covered by these circles in the actual experiments. Five clips (no. 1, 2, 5, 8, 10) were taken from TV programmes for young children "Okaasan to Issho" (NHK, Japan Broadcasting Corporation). Four (no. 4, 6, 7, 9) were taken from a film "Always: Sunset on Third Street" (Toho Co., Ltd). Clip no. 3 was taken from a film "A.I.-Artifical Intelligence" (Warner bros., not shown).

stimuli[16]. In addition, movements in not only the mouth but also the head are reported to provide information on the timing of speech and turn-takings in conversation[17,18].

We show here that our gaze behaviours did not much depend on the availability of sound, but were sensitive to time reversal. We further show that our face saliency model explained nearly 60% of the variance of gaze behaviours, and that the weights for the four components were dynamically adjusted depending on the direction of replay.

Results

Comparison of actual and artificial scanpaths. To characterize actual scanpaths recorded from individual participants (a time series of 1736 gaze positions for each participant), we compared them with several artificially generated scanpaths: "peak-face", "random-face", and "physical" saliency scanpaths. In viewing a frame shown in Figure 2a, most participants looked at the teachers in the centre and at the left female teacher in particular. As a result, the "peak-face" scanpath, defined as an artificial scanpath that followed the face with the largest number of gazes, fell on the face of the female teacher (orange dot). In contrast, a "random-face" scanpath, defined as an artificial scanpath that followed a face that was chosen randomly in each frame, fell on a boy in the right (red diamond), and a "physical" saliency scanpath (intensity channel), defined as an artificial scanpath that followed the peak of saliency in terms of low-level physical features defined by intensity, fell on the border of the black hair of a girl in the left against a white background (green square). The "peak" face scanpath seemed to represent the actual gazes of the 24 participants, but other artificial scanpaths did not.

This was generally true over the entire duration of the video stimuli, as indicated by the plots on the MDS plane (Figure 2b). Actual scanpaths (cyan and magenta symbols) clustered together, and the "peak-face" scanpaths fell near the centre of the cluster (orange symbols). In contrast, the "random-face" scanpaths (diamonds) and the "physical" saliency scanpaths (squares) fell in the periphery. Of particular importance, forward replay scanpaths (cyan circles) and reverse replay scanpaths (magenta triangles) formed two distinct clusters on the MDS plane, irrespective of whether the sound was available (filled symbols) or not (open symbols).

These observations were directly confirmed statistically by comparing the mean of within- or across-group distances (Figure 2c; one-way ANOVA, $F_{6,\ 6377} = 2885$, $p < 0.0001$). First, the mean distance between the "peak" face scanpaths and the actual scanpaths (Peak/Actual, 49 ± 20 pixels; mean ± *s.d.*) was significantly smaller than those calculated for the "random-face" (Random/Actual, 158 ± 9 pixels, $p < 0.0001$), and the "physical" saliency scanpaths (Physical/Actual, 157 ± 23 pixels, $p < 0.0001$). In addition, the mean distance between the actual scanpaths and the "peak" face scanpaths (Peak/Actual, 49 ± 20 pixels) was significantly "smaller" than the mean